EFDA–JET–PR(10)55

Yu.F. Baranov, C. Challis, J. Ongena, B. Alper, G. Arnoux, P. Buratti, T. Gerbaud, D. Keeling, V. Kiptily, J. Mailloux, M.-L. Mayoral, I. Monakhov, V. Parail, G. Sergienko, S. Sharapov and JET EFDA contributors

Large ELMs Triggered by MHD in JET Advanced Tokamak Plasmas: Impact on Plasmas Profiles, Plasmas Facing Components and Heating Systems

Large ELMs Triggered by MHD in JET Advanced Tokamak Plasmas: Impact on Plasmas Profiles, Plasmas Facing Components and Heating Systems

Yu.F. Baranov[1], C. Challis[1], J. Ongena[2], B. Alper[1], G. Arnoux[1], P. Buratti[3], T. Gerbaud[1], D. Keeling[1], V. Kiptily[1], J. Mailloux[1], M.-L. Mayoral[1], I. Monakhov[1], V. Parail[1], G. Sergienko[4], S. Sharapov[1] and JET EFDA contributors*

JET-EFDA, Culham Science Centre, OX14 3DB, Abingdon, UK

[1]EURATOM-CCFE Fusion Association, Culham Science Centre, OX14 3DB, Abingdon, OXON, UK
[2]Association "EURATOM - Belgian State", ERM-KMS, TEC partners, Brussels, Belgium
[3]EURATOM-ENEA Fusion Association, C.R. Frascati, CP65, 00044 Frascati, Italy
[4]Forschungszentrum Jülich, Institute of Energy Research - Plasma Physics, EURATOM Association, D-52425, Jülich, Germany
** See annex of F. Romanelli et al, "Overview of JET Results", (Proc. 23rd IAEA Fusion Energy Conference, Daejeon, Korea (2010)).*

Preprint of Paper to be submitted for publication in
Nuclear Fusion

ABSTRACT

Large ELMs triggered by MHD were observed in high β_N advanced tokamak (AT) plasmas in JET. They cause a considerable loss of the plasma thermal and fast particle energy (~10%) and an intensive plasma wall interaction, both of which affect the operation of additional heating systems. The ELM is followed by; a reduction in the electron and ion temperatures and toroidal rotation of the plasma, a rise in Z_{eff}; an anomalous decrease in the radiation temperature, and a sharp increase in the peripheral electron density. These features have been modelled to gain an understanding of the plasma behaviour associated with these ELM events. A large, toroidally asymmetric, increase in the neutral gas pressure outside the plasma was observed after such ELMs, which may cause arcs in the Lower Hybrid (LH) and Ion Cyclotron (IC) heating systems and increased reionisation in the Neutral Beam (NB) injectors. The heat load in the divertor was found to be small as a fraction of the plasma energy loss compared with regular type-I ELMs. Instead significant heating of the main chamber wall was observed. The implication of these events for the operation of AT plasma scenarios with high additional heating power will be discussed.

INTRODUCTION

Plasma wall interaction during type-I ELMs could play an important role in ITER [1,2]. Large ELMs triggered by MHD were observed in high-$\beta_N \approx 3$ advanced scenario discharges aiming at high fusion performance at reduced inductive current. These ELMs have distinctive features, which makes them different from regular type-I ELMs, observed in typical H-mode plasmas. In particular, such ELMs cause a relatively large (~10%) loss of the diamagnetic energy and considerable loss of the fast ion energy. Significant drops in electron and ion temperatures and over the plasma toroidal rotation in the entire plasma cross section were observed during these ELMs. Considerable, up to 100% increase in Z_{eff} was seen immediately after the ELMs due to the release of several of low and high Z impurities from the first wall [5]. In what follows the term MHD-ELM will be used to distinguish a large ELM triggered by MHD from a regular type-I ELM.

A fast increase by factor of 2 on the time scale of 100μs in the edge line integrated density is one of the most striking consequences of these ELMs. In addition, a strong decrease was measured on a time scale of 10 – 20μs in the radiation temperature T_{rad} of the Electron Cyclotron Emission (ECE): typically, T_{rad} dropped from several keV before the ELM to below 1keV during the ELM. A recovery of the T_{rad} to the post ELM steady state level was observed in several hundreds of microseconds after the ELM. Very short ($\tau \leq 10\mu s$) giant bursts of T_{rad} up to 10keV or even 1MeV were observed during MHD-ELMs.

We compared the heat load in the divertor during regular type-I ELMs and MHD-ELMs in advanced scenario pulses. The ratio of the heat load to the lost plasma energy was found to be significantly smaller for MHD-ELMs compared to the regular type-I EMLs. A significant step-like heating produced by MHD-ELMs was observed in the part of the wall in the main plasma chamber. Enhanced soft X-ray emission radiated by electrons with the kinetic energy above 2.2keV

was measured at the same location at the time of the MHD-ELMs.

MHD- ELMs were found to be deleterious for ICRH and LH systems as they often cause electric arcs and power trips in these systems. An anomalous rise in the pressure of the neutral gas was measured in the vacuum transmission lines (VTLs) of the LH, ICRH and NB systems after the ELMs. The pressure rise in the VTLs reflects the neutral gas pressure increase in the vacuum vessel. It is strongly asymmetric in the toroidal direction.

This paper is organised as follows: typical main plasma parameters in advanced scenario discharges with MHD-ELMs are presented in the first section, the effects of MHD-ELMs on the plasma temperature, toroidal rotation and Z_{eff} are discussed in the second section, ECE and interferometer measurements and electron density variation is demonstrated in the third section, the loss of the plasma energy and the heat load in the divertor and on the plasma-facing components during the ELMs are analysed in the fourth section. The effect of MHD-ELMs on the heating systems is discussed in the fifth section, which is followed by a discussion and conclusions.

1. PLASMA PARAMETERS IN ADVANCED SCENARIO DISCHARGES WITH MHD- ELMS.

Large MHD-ELMs were observed in high-β_N optimised shear pulses. Specifically, such events were found in hybrid scenario [3] and discharges with ITBs [4]. The phenomenology of the MHD-ELMs may slightly differ for these two groups of discharges. The most common and frequently observed MHD-ELMs observed in pulses with ITBs are described here to characterise the main features of the events. Plasma parameters are shown in Figure 1 for a typical high β_N discharge with ITB performed at magnetic field B = 2.7T and plasma current I_p = 1.8MA [4]. About 30MW of combined Neutral Beam (NB), Ion Cyclotron (IC) and Lower Hybrid (LH) power was applied in the early phase of the discharge (Fig.1a), when the q-profile was flat or slightly reversed. An ion ITB was formed in the vicinity of the q = 2 surface at t≈ 5s causing a rise in the plasma energy (Fig.1b) and neutron yield (Fig.1c). Two large MHD-ELMs occurred in this pulse at the time of the fishbone followed by bursts of pressure driven kink mode detected by the magnetic probe as shown in Fig.1 e and f. Both large ELMs are accompanied by a significant reduction of the diamagnetic energy and neutron yield (Fig.1b,c) and significant changes in the electron T_e and ion T_i temperatures, Z_{eff} and electron density n_e were observed after these ELMs.

2. EFFECT OF MHD-ELMS ON PLASMA TEMPERATURE, DENSITY, TOROIDAL ROTATION AND Z_{EFF}

Abrupt changes in the main plasma parameters caused by MHD-ELMs occur during a short time interval on the order of one millisecond. After that the plasma temperature, density and Z_{eff} vary on a diffusive time scale of the order of 10-50ms. The variation caused by large ELM (ELM1 in Fig.1 starts at t≈ 5.202s). Profiles of the electron and ion temperatures $T_{e,i}$, toroidal rotation Ω_{tor} , Z_{eff} and electron density before and after this ELM can be seen in Fig.2. The electron temperature profile

drops by 500-800eV throughout the full plasma cross section in 2.5ms (as will be discussed later the variation occurs on a time scale of the order of 100μs). This decrease in T_e is as large at the centre as at the periphery. Qualitatively, similar relative changes are also observed for the T_i, Ω_{tor} profiles as measured by the Charge eXchange (CX) diagnostic. Z_{eff} variation is much larger at the periphery than in the plasma centre. However, because of the time resolution of CX measurements variations in those profiles can only be measured every10ms. It should be noted that Z_{eff} measured by the CX diagnostic on JET reflects only the contribution of the Carbon impurity so it may significantly underestimate Z_{eff} in the presence of other light and heavy impurities. A small increase in the edge density was observed 10-15ms after the ELMs as shown in Fig.2e. For this discharge there were no data available at shorter time intervals after the ELM. A much larger electron density variation occurs immediately after the ELM on a shorter time scale as will be shown later.

The long term (~300-400ms) effect of large MHD-ELM on electron and ion temperature, toroidal rotation and electron density is shown in Fig.3. A contour plot for each parameter contains a gap because there are no valid measurements for these parameters at the time of the ELM. Thompson scattering and charge exchange measurements are affected by parasitic emission (D-alpha light) and the ECE emission is distorted by non-thermal effects and a black-out due to density cut-off, as discussed in section 3. At the time of the ELM $t = t_{ELM}$, abrupt changes in the plasma edge are seen for all parameters shown in Fig.3. A discontinuity in T_e is clearly visible and similarly for T_i, Ω_{tor} and n_e. While the electron and ion temperature and the toroidal rotation drop at $t = t_{ELM}$, the electron density profile rises and the electron density gradient at the boundary increases. There is a clear sign of a "cold pulse" [6] propagation from the boundary to the plasma centre triggered by the ELM, which leads to a gradual reduction of T_e, T_i and Ω_{tor} on a diffusive time scale of the order of 50ms. Plasma parameters recover to the pre-ELM level in 400-500ms, which involves an ITB reappearance in the vicinity of the $q = 2$ magnetic surface. The time of the recovery is probably connected to the current diffusion time required to re-establish the q-profile favourable for ITB formation.

Bremsstrahlung emission measurements indicate a strong and abrupt increase in Z_{eff} as shown in Fig.4c [5]. In contrast to CX, the bremsstrahlung emission measures a contribution to Z_{eff} from all impurities. The increase in Z_{eff} is triggered by both large MHD-ELMs indicated in Fig.1. Spectroscopic measurements show that there is a considerable influx of low and high Z impurities (Fig.4a,b). Laser ablation of the nickel target was done at $t = 6s$ to study the diffusion of the heavy impurities. There is a strong increase of the Ni lines at $t = 6s$, but only a small perturbation to the Z_{eff} deduced from the bremsstrahlung emission. Both low Z impurities like Carbon, Nitrogen and Oxygen as well as high Z impurities like Copper, Nickel and Chromium all contribute to a considerable increase in Z_{eff} caused by the two large MHD-ELMs. Remarkably, no increase is visible in the intensity of the Iron lines in this case (see line Fe24 in Fig.4a), which is usually associated with electric arcs in the LH launcher. The surface of the NB ducts and the LH launcher are covered with a Copper layer and Nickel is part of the vacuum vessel wall material. Clearly, there is an intense interaction with plasma-facing components during large ELMs causing plasma contamination.

3. EELECTRON CYCLOTRON EMISSION AND INTERFEROMETER MEASUREMENTS DURING LARGE MHD-ELMS.

A peculiar behaviour of the radiation temperature T_{rad} was observed during large MHD-ELMs. The radiation temperature was measured by a 96-channel ECE heterodyne radiometer at the frequency of second electron cyclotron harmonic of the X-mode. Figure 5a shows a contour plot of T_{rad} as a function of the major radius and time. Before the ELM the plasma is optically thick ($\tau_{op}>>1$) and $T_{rad} \approx T_e$, where $\tau_{op}(r, a) = 2\int_r^a \mathrm{Im}(k_\perp(r'))dr'$ and $k_\perp$ is the component of the wave vector perpendicular to the magnetic field. The minimum temperature is at the separatrix located at R_s=3.76-3.8m, which is marked by yellow colour in Fig.5a. The edge transport barrier (ETB) associated with H-mode is in the vicinity of the separatrix. T_{rad} increases in the region of small optical thickness ($\tau_{op}<<1$) beyond the sepatatrix [7]. A fishbone mode is excited initially [8] in the vicinity of the ion ITB base at R = 3.55m [8]. The phase of the T_{rad} perturbation is a continuous function of R and it corresponds to the kink like mode (in contrast to the tearing like mode, where the phase experiences a π-shift inside the zone where the mode is localised). The radial excursions of the T_{rad} = const surfaces increase with time. The temperature gradient inside the separatrix varies; it increases, when T_{rad} = const surfaces expand radially and decreases in the opposite phase during first three period of the MHD perturbation. The plasma inside the separatrix is well isolated from the plasma outside SOL. During the forth period of the MHD perturbation ETB is "punctured" for a short time interval but it recovers. The plasma probably loses some energy at this time and it causes a very fast shift of the separatrix by about 2-3cm inward. One can see a sudden reduction in T_{rad} inside the separatrix at t = 5.20174s. About 20μs later there is a fast expansion of T_{rad} = cons surfaces. After that a complete collapse of T_{rad} occurs and it drops to a very low level below 1keV in time interval 5.201782s-5.201788s. This process is illustrated in Figure 5a,b and c. T_{rad} remains very low for more than 1ms as can be seen from Fig.6a and b. Then it starts to recover. It should be noted that T_{rad} rises first in the region of smaller R or larger cyclotron frequencies $\omega_{ce} = eB(R)/mc$ and then at larger R or smaller ω_{ce} (see Fig.6a,b). The time of the emission recovery is on the order of 1ms.

The reduction in the electron temperature in the entire plasma cross-section from the several keV to below 1keV in a dozen of microseconds would normally cause the radiation collapse and production of run-away electrons etc, which is not consistent with our observations. The electron heating needed to recover T_e=T_{rad} after the ELM would mean an energy increase in the electron component from a very low level to about 2MJ in 1ms time, corresponding to a heating power of 2GW. This is about three orders of magnitude larger than the available power. The soft X-ray emission contour plot is shown in Figure 7 as measured by the horizontal camera, which registers a radiation in the energy range of 2.2-12keV and mainly from the plasma core. It shows that the abrupt change in the soft X-ray emission begins at the start time of the ELM, which is defined as the moment of D_{alpha} signal rise. This moment coincides roughly with the abrupt T_{rad} collapse discussed above. This variation in the soft X-ray signal continues for about 200-300μs. After that

the soft X-ray emission remains constant during the time interval t=5.202-5.204s, when T_{rad} is either very low or recovers (see Figures 5,6). This clearly shows that both the electron temperature T_e and electron density n_e in the plasma core remain stable during this period of time. This means also that the radiation temperature during the ELM does not represent the electron temperature. There are at least three mechanisms that could reduce T_{rad} during the ELM: an increase in the electron density to the cut-off level, ECE emission scattering by density fluctuations and formation of a non-Maxwellian electron distribution function. The first mechanism is considered to be the most realistic as it is supported by the data. The two other mechanisms mentioned can play an important role under certain conditions, which are not fulfilled during the ELMs.

The reduction in T_{rad} is observed when the electron density reaches the cut-off level in high density pulses. Qualitatively it looks very similar to the behaviour of T_{rad} during the large MHD-ELMs discussed here. If the ECE emission at the second harmonic of the X-mode comes from the point R then the cut-off density at the radius R_c>R can be expressed through the toroidal magnetic field B_o at the plasma centre R_o as: $n_{cut\text{-}off}(m^{-3}) = 3.89\times10^{19}\,(B_o(T)R_o/R)2\,(1-0.5R/R_c)$. Note that the expression for the cut-off density was neglects a contribution of the poloidal field to the total magnetic field. It is natural to suggest that the black-out of the ECE emission in our case happens due to the density increase caused by the plasma wall interaction during the ELM. We assume that the increase in electron density occurs near the separatrix location. The radial dependence of the $n_{cut\text{-}off}$ is shown in Figure 8 for Pulse No: 78085 at t=5.2s assuming that R_c=3.8m (the graph shows only the region covered by the heterodyne radiometer). The plasma becomes non-transparent for ECE emission coming from the point at R = 2.7m if electron density is above $2.05\times10^{20}m^{-3}$ at $R = R_c$ = 3.8m and the cut-off density decreases to $0.84\times10^{20}m^{-3}$ for the emission coming from R = 3.8m. To explain the T_{rad} evolution in time and space (Fig.5,6) one needs to assume that electron density in the vicinity of the separatrix and in front of the antenna horn receiving the ECE emission rises to a level $2.6\times10^{20}m^{-3}$ during the ELM and remains at this level or above it until 5.2034s. After that the density gradually decreases. The plasma becomes transparent for the X-mode second harmonic ECE emission starting from highest frequencies or smallest R (see gradual transition from profiles 2 to 5 in Fig.6b).

Comparing the temperature perturbation observed during pellet fuelling experiments with the T_{rad} perturbation in this discharge we conclude that there were no macro particles penetrating in the plasma before or during the MHD-ELM. We assume therefore that the increase in electron density during the ELM is due to plasma wall interaction causing a massive injection of neutral particle.

Sharp rise of the line averaged density $\bar{n}_eL = \int n_e dl$ is observed during large MHD-ELMs (Fig.9.a). It is especially pronounced in the edge vertical channel #4 located at R = 3.75m (the magnetic axis and the separatrix are at R_m = 3.-3.1m and R_s = 3.8-3.85mfor the discharge considered here). In some cases the line integrated density $\bar{n}_eL$ increases by factor of 2 and more for this channel. The rise time is of the order of 1ms in channel #4 and slightly longer in other more central channels

(Fig.9a). Fast interferometer data show that the line integrated density (channel #4) rises in about 100μs. The decay time of $\bar{n}_e L$ is of the order of several ms in the edge channel #4 and slightly longer for the central channels. The line integrated density decreases after the ELMs back to the initial level in 15-20ms (Fig.9a). A large and only modest increase in $\bar{n}_e L$ for, respectively, edge and central lines of sight indicates that the relative rise in electron density is greater at the periphery than in the centre.

The density variation caused by a short in time and a large deuterium gas puff was modelled using the JETTO code [9]. It was assumed for simplicity that T_e and T_i varied during 2.5ms (the MHD-ELM duration), respectively, from profiles 1 to profiles 2 as shown in Fig.2a,b. The gas puff was increased from the experimental level of 3×10^{22} electrons per second before the ELM to a value which allowed us to reproduce the line integrated density variation in channel #4 in a time interval of about 500μs. Experimentally, the density rise time τ is shorter than 500μs, but numerical problems prevented us from shortening τ. The calculated electron density is shown in Fig.10, obtained with a total gas flux of 5×10^{24} electrons per second during the density rise, particle diffusion $D=1m^2/s$ and zero convection velocity.

The evolution in time of the measured and calculated $\bar{n}_e L$ is shown in Figure 9a. It should be noted that the profiles shown in Fig.10 are indicative only as the result of the modelling depend on the assumed particle diffusivity, convection, energy of the neutrals coming from the wall (3eV in the modelling) etc. The gas flux of 5×10^{24}el/s is a minimum amount required to provide the observed $n_e L$ in the channel #4. In reality it should be even larger because the measured density rise time is shorter than in the modelling and the particle diffusion coefficient and convection velocity chosen for the modelling are most likely too small. Clearly, the neutral gas particles penetrate only in a narrow plasma layer near the separatrix as can be inferred from Fig.10 and the electron density perturbations inside $r/a<0.9$ are relatively small. It should be noted that the evolution of the density and temperature outside the separatrix were ignored in the modelling, although in reality the density build up may occur exactly in this region. Figure9a shows that the density profiles obtained in the calculation are roughly consistent with the measured $\bar{n}_e L$ variation only for channel #4. To explain the discrepancy in the other channels we need to assume that the density profile shows large poloidal inhomogeneities. These are closely connected to the toroidal inhomogeneities, which are well pronounced and will be discussed in section 5.

Figure 11a shows a contour plot of the radiation temperature for a short time interval just before and during the start of the second large MHD-ELM (ELM2 in Fig.1). The ELM start time is defined as D-alpha signal rising time. It is triggered by a global kink-like mode. Two periods of this mode are clearly visible in Fig.11a. Two important facts can be deduced from the graph. High frequency (f = 20-60kHz) MHD is excited in the region of R = 3.4-3.6m at t = 6.4435s and the maximum of T_{rad} perturbation is around R = 3.55m or $r/a \approx 0.6$. The perturbation amplitude increases and it spreads toward the plasma edge after t = 6.4435s. The separatrix and ETB were well defined at $R \approx 3.78$m until t = 6.4435s. After that the ETB is eroded by the MHD and disappears.

The edge barrier is, probably, destructed by a stochastisation of the magnetic field in the separatrix region. The MHD is excited far from the plasma boundary (r/a<0.7) and then moves towards the edge. Theory predicts [10],[11] that ELMs are triggered by ballooning or peeling like modes. The maximum of their eigenfunctions is typically closer to the plasma edge (r/a>0.8).

Large bursts of non-thermal ECE emission are observed during MHD-ELMs. Usually this emission is detected in the form of short bursts during ELMs. In the contour plot of Fig.11a a small black-blue "island" at R = 3.5-3.65m and t=6.44353s represents such a burst. The profile of T_{rad} at the time of the burst is shown in Fig.11b. The duration of the burst is on the order of several microseconds. Profiles of T_{rad} before and after the burst are smooth and monotonic. Non-thermal emission of this amplitude is always observed from the plasma in current drive experiments with several MW of LH power. Using LHCD this emission is created by energetic electrons (E=70-100keV) carrying a current of several hundreds of kA. The main difference between the non-thermal emission in the case of Fig.11b and in the case of LHCD plasma is the localisation of the non-thermal emission. T_{rad} in the LHCD case reaches its maximum beyond the separatrix in the low field side region (see details in [12]).

The connection between energetic electrons and the non-thermal ECE emission associated with ELMs becomes clear if one takes into account the dependency of the emission frequency on the electron energy. The cyclotron emission frequency of a particle located at R is $\omega_{ce}^{\ 1} = \omega_{ce}^{\ 0} / \gamma$, where $\gamma = (1-(v/c^2)^{-1/2}$ is the relativistic factor, $\omega_{ce}^{\ 0} = eB_0R_0$ is the local cyclotron resonance frequency, m is electron rest mass, v and c are particle velocity and speed of light, respectively. That means, for example, that electrons located at the centre of the zone of high T_{rad} at R = 3.6m (see Fig.11a,b) with energy 50-100keV (γ = 1.1-1.2) contribute to T_{rad} at $R = \gamma R^1$ = 3.96-4.32m. Secondly, a comparison with the LHCD plasma shows that a considerable amount of fast electrons is required to create significant increase in T_{rad}, which is difficult to expect in the case of the MHD-ELM. Thirdly, it is difficult to accelerate electrons to high energy during a short time interval of the order of several microseconds and it is even more difficult to stop them in a short time due to their low collisionality. It should be noted in addition that in many cases the non-thermal emission bursts are of much bigger amplitude than what is shown in Fig.11, and several cases where max(T_{rad}) reaches several hundreds of keV have been observed. A possible explanation of the burst of the EC emission is connected to a strong modification of the electron distribution function. Discussion of this problem is beyond the scope of our investigation.

4. PLASMA ENERGY LOSS, RADIATION AND EFFECT ON A DIVERTOR

In the discharge considered, the plasma loses about 10–12% of its diamagnetic energy during both large MHD-ELMs (see Fig 12b). The duration of the energy loss according to the fast diamagnetic signal is on the order of 400μs or shorter, which is similar to the time variation of the electron temperature deduced from the soft X-ray measurements as shown in Fig.8. The radiation losses in the plasma were estimated from the bolometer measurements. The total radiated energy and

energy radiated in the divertor during 5ms from the start of the ELM make up about 8% and 5% of the total diamagnetic energy. The Scintillator Probe (SP) [13,42] located in the shadow of the limiter registers a sharp increase in the fast ion losses with energies 250keV $<E_{fi}<$ 3.MeV during a short period of time of the order of about 1ms. The SP detects mainly the first orbit losses of hydrogen H^+ and deuterium D^+ accelerated by IC waves and fusion products of D-D reaction such as T^+ and protons [14]. It takes about 1μs for the ions to reach the SP from the plasma core. Surprisingly, the losses are detected about 100μs after a rise in D-alpha signal, drop in T_{rad} and a sharp reduction in the MHD activity (Fig12d,e,f), Such delay makes the losses of the fusion products and ICRH accelerated ions an unlikely candidate for a release of the neutral gas from the first wall. A correlation between an increase in fast ion losses and an increase in the impurity content and Z_{eff} was reported previously [5] and the fast ion losses discussed in ref. [5] were always caused by large ELMs triggered by MHD. However, in this case, the increase in Z_{eff} does not always correlate with a significant increase in the scintillator probe signal. This could possibly be explained by an asymmetry in the fast ion losses, which are connected to the toroidal asymmetry of the plasma wall interaction that will be discussed in the next section.

According to the TRANSP [15] modelling the electron heat flux averaged over 100ms before large MHD-ELM (ELM1 in Fig.1) is equal to 0.04MW/m^2. The electron energy content of the plasma within r/a≤0.9 decreased from 2.37MJ before to 2MJ after the ELM. As shown in Section 2, the decrease in the electron energy occurs during approximately 200-300μs. The heat flux associated with such a loss is equal to 18-27MW/m^2, which is about two or three orders of magnitude larger than the average electron heat flux before the MHD-ELM. Losses in the ion energy content are more difficult to assess as there is no detailed information on the evolution of the T_i during the ELM. The plasma energy lost during this short time interval is the main source of the energy required to ionise the neutral gas released from the wall.

The soft X-ray emission in the energy range of 2.2-12keV measured by the vertical camera during the large MHD-ELM is shown in Figure 13 (despite the fact that the absolute value of the soft X-ray emission in the different channels is not correct, the relative time differences between the channels can be trusted). Two bright spots appear at the time of the T_{rad} collapse and last for about 300μs. Similar spot of smaller amplitude can be seen in Fig.8 measured by the horizontal soft X-ray camera. This enhanced radiation occurs in two vertical and one horizontal lines of sight shown in Figure 13b. These lines cross the top of the vacuum vessel (point 5), outer divertor plate (point 6) and the tile above the inner divertor plate (points 1). A signal from channel 20 of the vertical soft X-ray camera is shown in Fig.12g. This signal starts to rise simultaneously with the D_α signal at the time when regular n = 1/m = 2 global kink mode is fragmented into higher m/n and higher frequency modes (Fig.12d, 6a). The bright spots in Figure 8 and 13a are produced by electrons hitting the wall or target plate in the vicinity of the points 1,5 and 6 indicated in Fig.13b. The energy of these electrons is above 2.2keV.

The temperature variation on the target plates of the divertor are measured by the fast infrared

camera [16]. The power and the heat flux are deduced from these data. The power dissipated on the outer plate P_{od} is considerably larger than on the inner plate. It is instructive to compare the power and heat flux variations during large MHD-ELM and regular (periodic) type-I ELMs. The time evolution of the D-alpha signal, diamagnetic energy and radiated power are shown in Fig.14 for a number of periodic type-I ELMs, which are followed by large MHD-ELM (ELM1 in Fig.1). The loss of the diamagnetic energy ΔW_{dia}, total E_{rad} and energy radiated in the divertor E_{drad}, energy dissipated on tile 5 of the outer divertor plate E_{t5} and its maximum temperature are given in the Table 1 for a regular type-I ELM and large MHD-ELM (ELM1) marked by the dashed line in Fig.14. The diamagnetic energy lost during the regular ELM is 2.5 times smaller than during the ELM1. However, the maximum temperature near the strike points on the divertor plates is larger for the small ELM than for the large ELM1, as shown in Table 1. In Fig.15a we compare for tile 5 the total dissipated power P_{t5}, radial profiles of the heat flux Γ_{t5} and max(Γ_{t5}) during the two selected ELMs. The energy dissipation E_{t5} is approximately the same for the first 1.5ms from the start of each ELM (see Table 1). Note that in a standard H-mode discharges the power dissipated on tile 5 during a type-I ELM increases with increasing losses in the diamagnetic energy ΔW_{dia} [17]. The time variation of the total dissipated power P_{t5} becomes practically identical in 400μs after the start of the large and regular type-I ELM. The maximum of the heat flux is larger on average in the regular type-I ELM (Fig.15b). The wetted area defined as A= P_{t5}/max(Γ_{t5}) is close 0.3m^2 between ELMs. It rises to 0.7-0.8m^2 during regular type-I ELMs and to 1.4m^2 during a large MHD-ELM. The radial extent of the heat flux Γ_{t5} is larger in the case of a large MHD-ELM as demonstrated in Fig.15,c,d.

The infrared camera provides a wide angle view of the vacuum vessel as shown in Fig.16a. The surface temperature variation at four points marked in the figure is shown in Fig.16b. Notably, there are two significant jumps of about 200-250 degrees C in the temperature at the points 1 and 2, which occur immediately after the two large MHD-ELMs (ELM1 and ELM2 in Fig1). Points 1-4 in Fig.16 coincide with the corresponding points in Fig.13b. The locations of the divertor inner and outer strike points coincide with points 2 and 3, respectively. Point 4 is on the septum of the RF antenna B. A strong increase in the soft X-ray emission was observed at point 1 at the start time of both large ELMs as discussed previously (Fig.13). The effect of the heating produced by the two MHD-ELMs is long lasting at the points 1. The time averaged effect of the MHD-ELMs is smaller at the outer strike point 3 than at points 1 and 2. The surface temperature at the bright spot 4 (Fig.16a and Fig.13b) on the RF antenna septum is not influenced by the large MHD-ELMs. Temperature here decreases after these two ELMs. Similar temperature behaviour is observed on the surface of other septa and limiter seen by the camera (Fig.16a).

The fact that the energy losses E_{t5} in the outer divertor during large MHD-ELM is comparable to the losses during regular type-I ELM, when ΔW_{dia}(MHD-ELM)>> ΔW_{dia}(type-I-ELM) indicates that there are considerable additional losses in the main chamber in the case of large MHD-ELM as compared to regular type-I ELM. The excitation and ionisation of the neutral gas released from the plasma facing components during the MHD-ELM leading to very large density increase at the

plasma periphery is one of such channels. It is required above 36kJ to create peripheral plasma layer shown in Fig.10. Exact number depends on the rate of plasma recombination and particle losses from the layer and may significantly exceed this value. The losses should be considerable especially in the region outside the separatrix, where the plasma build up, probably, occurs. The recombination may play a significant role also in the peripheral layer as the plasma density is expected to be large ($n_e > 10^{20} m^{-3}$) and temperature low (T_e~eV) due to a presence of large number of cold neutral particles. This energy required to create the peripheral dense layer should be derived mainly from the energy lost by electrons in the first 100 μs (time of the density rise) of the ELM duration. This energy is comparable to the entire energy dissipated on the outer target plate during 1.5ms (see Table 1).

The observed temperature reduction on the surface of the RF antenna septa and limiter (Fig.16a, b) can be explained by increase in the antenna plasma distance and screening of the septa and limiter by cold and dense plasma formed at the edge during large MHD-ELMs.

5. EFFECT ON THE HEATING SYSTEMS

Large MHD-ELMs may cause trips of the ICRH and LH systems. A typical example of such trips is shown in Fig.17c and e for pulse #78085.The LH system was completely stopped by the protection system due to large level of radiated power detected by the bolometer (Fig.14d). This radiation was above the radiation limit and poloidally asymmetric in the vicinity of the LH antenna. Such radiation is associated with an electric arc in the LH grill mouth in the absence of large MHD-ELMs. Usually the arc in the LH launcher releases iron from the wall of the waveguides and it leads to a large increase in the poloidally asymmetric emission of the iron lines Fe XXIII- XXIV from the plasma. Such lines have only rarely been observed in cases associated with large MHD-ELMs (see e.g. Fig.4a). The poloidal asymmetry and intensity of the radiation during large MHD-ELM is connected to the localised nature of the plasma wall interaction and large influx of the neutral particles released from the plasma facing component. The protection system was designed to stop LH power in the case of electric arcs. The system failed to distinguish between large MHD-ELMs harmless to the LH system and electric arcs causing damage to the LH launcher.

Figure 17f shows the pressure of the neutral gas inside the LH launcher. The pressure gauge is located about 3m from the grill mouth. There is a time delay of around 50ms between the start of the MHD-ELM and the time when the pressure rise begins. The pressure increase inside the launcher after large ELMs in the absence of an arc is associated with the pressure rise of the neutral gas inside the vacuum vessel. The time delay is connected to the finite time required for the neutrals to reach the location of the pressure monitor from the vacuum vessel.

The ICRH power is often tripped by ELMs. In the case of large MHD-ELMs there are additional features in the behaviour of the ICRH. The coupling resistance R_c of the ICRH antenna and the signal of the magnetic probe are shown in Fig.18 before and during the MHD-ELM in Pulse No: 78085. The MHD modulates the electron temperature (Fig.6a) and density. Such modulation causes

a fluctuation in R_c which follows the amplitude and the phase of the MHD (Fig.18). The coupling resistance rises to a large value approximately at the time of the T_{rad} collapse which reflects a very fast rise in electron density in front and in the vicinity of the ICRH antenna. An electric arc results, probably, from the density rise inside the antenna. The protection system trips the ICRH system. These power trips are clearly visible in Fig.17c at the time of the two MHD-ELMs. The neutral gas pressure is measured inside the RF Vacuum Transmission Lines (VTL) at a distance of about 3m from the plasma. The gas pressure increases considerably after the two MHD-ELMs (Fig.17d) considered with the time delay of about 25ms. There is a noticeable asymmetry in the pressure for different antennae. The pressure rise in the VTL of antennae A and B located between octants 1 and 3 is significantly larger than that in the antennae C and D located between octants 5 and 7. The relative pressure increase varies in different pulses for different antennae.

The NB system consists of two modules located in octants 4 and 8 on the opposite sides of the torus. The neutral gas pressure is monitored in the ducts and rotary valves of this system. Figure 17a and b show the NB power and the neutral gas pressure in ducts and rotary valves for Pulse No: 78085. A significant pressure increase in the duct of octant 8 follows each MHD-ELM. A slightly smaller increase occurs in the rotary valve of octant 8. The difference in the time evolution of the neutral gas pressure in duct and rotary valve results from the fact that the flux of neutral gas from the vacuum vessel penetrates the rotary valve through the duct.

A short perturbation of the neutral gas pressure in the duct caused by an MHD-ELM can be roughly approximated as $\nabla P = G \times \exp(-\tau/\tau_d) \times (1 - \exp(-\tau/\tau_r))$, where $\tau = t\text{-}t_{0,}$ with t_0 the start time of the perturbation, G is a constant proportional to the amplitude of the perturbation, τ_r is the rise and τ_d decay time of the pressure perturbation.

The perturbation measured by the pressure gauge can be expressed as follows:

$$\Delta P_g = P_g - \langle P_g \rangle = G \times \exp(-\tau/\tau_g) \times [(\exp(-\tau/\tau_1) - 1)\ \tau_1/\tau_g - (\exp(-\tau/\tau_2) - 1)\tau_2/\tau_g]$$

where $\tau_1 = \tau_g \tau_d / (\tau_d/\tau_g)$, $\tau_2 = \tau_d \tau_r \tau_g / (\tau_d \tau_r - \tau_r \tau_g - \tau_d \tau_g)$ and $\langle P_g \rangle$is the measured pressure averaged over a time interval longer than the perturbation time. The time constant τ_g characterises the integration time of the pressure gauge. For the gauge considered here, we used $\tau_g \sim 0.14$s. The perturbation rise τ_r and τ_d decay times are not arbitrary. They depend on the time dependence of the recorded pressure ΔP_g.

The recorded gauge pressure starts to rise 20ms after ELM1 (Pulse No: 78085) and reaches its maximum at 90ms after ELM1 (Fig.17b). From the expression for ΔP_g and the measured data shown in Fig.17 we find that for $\tau_r \rightarrow 0.0$s $\tau_d \approx 0.04$s, $P = 5.6\ \Delta P_g$ and for $\tau_r \rightarrow 0.05$s $\tau_d \approx 0.023$s $P = 3.9\ \Delta P_g$. It shows that for short perturbations ($\tau_r, \tau_d < \tau_g$) the actual pressure increase ΔP is considerably larger than the measured increase ΔP_g. If the pressure perturbation becomes longer than the gauge integration time ($\tau_r, \tau_d > \tau_g$) then $\Delta P \rightarrow \Delta P_g$. It should be noted that the large increase in neutral gas pressure in the duct of the NB system is undesirable, as it may cause a reduction in the NB power and damage to the duct walls. (Beam particles may re-ionise due to collisions with neutral

gas particles. They are deflected by the magnetic field and hit the duct walls causing overheating and destruction of the wall material). The NB protection system trips the power to prevent such damage. Figure 19 shows an example of such an event in Pulse No: 77587. A large MHD-ELM caused influx of neutrals in the vacuum vessel in this pulse. A burst in the D_α signal measured along the midplane line of sight is much larger than along the vertical line of sight looking into the divertor. Part of the neutrals penetrated the duct in octant 8. The neutral gas pressure increased above the protection limit and it caused a trip in the NB system in octant 8. We want to stress the fact that the duct pressure and NB power in octant 4 remained unaffected by the ELM, which indicates that the perturbation caused by the ELM is strongly asymmetric in the toroidal direction.

A similar toroidal asymmetry in the neutral gas pressure increase is observed in pulse #78085: it is larger in octant 8 than in octant 4 after both large MHD-ELMs (Fig.17b). Comparing the data from the ICRH system with the data from the NB system one can conclude that in this pulse the neutral gas pressure rise is larger in that part of the torus that includes octants 8-1-2-3 and smaller on the opposite side including octants 4-7. However, an increase in the pressure of the neutral gas and the asymmetry changes from pulse to pulse. For example, there are cases when the pressure increased predominantly in octant 4 with only a small effect in octant 8 and cases with the pressure rising in both octants.

SUMMARY AND DISCUSSION

The effect of large ELMs triggered by MHD (MHD-ELMs) in advanced scenario pulses in JET has been analysed. MHD-ELMs typically occur in high β_N~3 discharges with high NB and ICRH heating power of the order of 20-30MW. Pressure driven kink-like mode is excited in such pulses and becomes global in several periods of the mode evolution. The amplitude of the plasma displacement reaches large amplitude of the order of $\delta/a \sim 0.2\text{-}0.3$ (Fig.5,11). The mode modulates the pressure gradient inside the separatrix and may cause a temporal and partial loss of the plasma energy and a small inward shift in the position of the separatrix (Fig.5). The non-linear evolution of the original kink-like mode leads to the development of high frequency (f = 20-60kHz) perturbations clearly seen on the magnetic signals and on the radiation temperature (Fig.5,12d). These high frequency perturbations are formed in the region of $r/a \sim (0.5\text{-}0.7)$ during about the last two periods of the kink-mode evolution before a crash. These modes expand towards the plasma boundary and cause a destruction of the ETB and the separatrix. At the same time the magnetic signal increases and becomes non-periodic (Fig.12d), the soft X-ray emission produced by electrons with E>2.2keV increases in several points outside the divertor (Fig.13a), the D-alpha signal and the edge density increase (Fig.9) and the radiation temperature drops to a very low level (Fig.5b,c).

The plasma loses around 10% of its diamagnetic energy in about 400μs or faster (Fig.12b) during large MHD-ELMs. The electron component loses its energy in about 200-300μs, according to soft X-ray measurements (Fig.7). Electron and ion temperatures and toroidal rotation drop in the entire plasma cross section by 5-10% during the MHD-ELM (Fig.2). If the ITB existed before

the MHD-ELM, it shrinks radially. Z_{eff} increases abruptly due to the penetration of several light and heavy impurities (Fig. 2d, 4). The plasma is cooled at the edge and the temperature gradients are reduced (Fig. 2a,b). The entire plasma boundary is shifted by 2-4cm inward. The cold pulse propagates after the MHD-ELM from the edge to the magnetic axis on the time scale of the heat diffusion time of about 50ms (Fig.3). The electron temperature decrease and Z_{eff} increase cause a redistribution of the plasma current, which evolves on the current diffusion time. In the presence of the high power heating the ITB can be re-established in 400-500ms after the MHD-ELM (Fig.3).

The interaction of the plasma particles with the plasma-facing components causes a release of a very large number of neutral particles. This number is higher than in the case of regular type-I ELMs. It is not clear, what plasma component is mainly responsible for the release of neutrals. The increase in the soft X-ray emission is indicative of an enhanced loss of fast electrons with energy above 2keV and there is a localised interaction of these lost electrons with the wall coinciding with the increase of the D-alpha signal (Fig.12f,g). Such interaction may cause efficient out-gassing of the first wall. The Scintillator Probe (SP) signal indicates that enhanced first orbit losses of the fast H^+, D^+ and T^+ ions produced by ICRH and born in D-D fusion reactions occurs during large MHD-ELMs (Fig.12). These losses are toroidally asymmetric. Such losses appear mostly due to abrupt redistribution of the fast ions from the confined orbits to unconfined trapped orbits [18]. The energy of the lost ions detected by the SP is of the order of 1MeV. The ions are lost in about 1μs after the orbit change on the first leg of their trajectory from the core to the plasma boundary. There is a time delay of the order of 100-200μs between the maximum of the magnetic probe, D-alpha signals and the SP signal. This time delay is too large in comparison with the time of the first orbit loss of the fast ions, if such loss is caused by original kink-mode perturbation. The fast ions losses registered by the SP are unlikely to play a significant role in the release of the neutrals from the wall and build up of the electron density at the plasma edge. The role of the beam ion losses is unclear as their energy is of the order of 100keV and they are not registered by the SP.

Large and abrupt increase in the neutral flux from the plasma-facing components and release of a significant amount of the plasma energy cause intensive excitation and ionisation of the neutrals and electron density build up at the edge registered by the interferometer (Fig.5a). The maximum of the electron density at the edge may increase up to $(2\text{-}3)10^{20}m^{-3}$ equivalent to a factor of about 5 compared to the maximum of the central electron density (Fig.10). The edge electron density increases above the cut-off density $n_{cut\text{-}off}$ for the second harmonic of the X-mode ECE emission (Fig.9). It causes a sudden black-out of the emission and a reduction in the radiation temperature (Fig.5). This plasma state with enhanced edge electron density exists for about 10-1000μs (the duration depends on the amount of the neutral gas released from the wall, location of plasma wall interaction etc.). During the time of the black-out the edge electron density in front of the ECE diagnostic antenna horn drops to a level below the cut-off density and the T_{rad} profile recovers. The recovery occurs first in the region of higher magnetic field (higher $n_{cut\text{-}off}$). Short (~5μs) bursts of the ECE emission with an effective radiation temperature in the range of several keV to 1MeV have

been observed during MHD-ELMs (Fig.11). These bursts result from the strong modification of the bulk of the electron distribution function and have no relation to the suprathermal electrons (Section 3).

We also investigated the plasma energy loss and the effect of regular type-I ELMs and large MHD-ELMs on to the plasma-facing components in the main chamber and in the divertor. It was found that the total energy heat flux to the outer target plate E_{t5} (tile 5) and the diamagnetic energy loss from the plasma ΔW_{dia} is 1.2 times and 3 times larger for MHD-ELM than for the regular type-I ELM, respectively (Table 1, Fig.15a). The smaller increase in E_{t5} (kJ) compared to the increase in ΔW_{dia} can be explained by relatively large energy loss needed to ionise and excite neutrals in the case of large MHD-ELM. It is even more curious that the maximum heat flux at the strike point is close or even larger for regular type-I ELM (Fig.15b,c and d). The IR camera shows significant heating with a long lasting effect (~0.5s) produced by large MHD-ELMs in the main chamber above the divertor. The heating occurs at the location where enhanced soft X-ray emission is observed at the start of the MHD-ELM (Fig.16, 13b). The heating is similar in amplitude, but of a shorter duration (~0.1s) and is observed in the vicinity of the inner strike point. There is no pronounced "afterglow" at the location of the outer strike point (Fig.16, 13b). It is remarkable that the septum of the ICRH antenna experiences a relative cooling down during and after large MHD-ELMs. This can be explained by a screening of the antenna and its septum from the bulk of the plasma by a dense and cold plasma layer produced by the MHD-ELM. The inward shift of the separatrix during and after the MHD-ELM may also play an important role (Fig.2,3).

Large MHD-ELMs in advanced scenario discharges may affect the functioning of the heating systems. The neutrals released during the MHD-ELMs from the plasma-facing components penetrate from the vacuum vessel to the ducts and rotary valves of the NB system. Significant increase of the neutral gas pressure was registered after large MHD-ELMs in these elements of NB system (Fig.17a,b). The real pressure increase after the MHD-ELM is considerably larger than the pressure gauge reading due to the integration properties of the pressure monitor (see Section 5). Enhanced pressure in the ducts of the NB system may reduce its efficiency and damage the duct walls.

The ICRH antenna coupling is strongly affected by large MHD-ELMs. The coupling improves during the first 20-30μs from the start of the ELM, when the edge density increases. Then an electric arc occurs and the protection system trips the RF power (Fig.17c). A significant rise in the neutral gas pressure after large MHD-ELMs is registered by monitors located in the coaxial transmission lines at about 3m from the plasma boundary (Fig. 17d).

The pressure increase recorded in NB and ICRH systems is typically asymmetric in toroidal direction, which indicates a toroidal and possibly poloidal asymmetry in the plasma wall interaction during large MHD-ELMs.

The LH system was often stopped by MHD-ELMs due to large radiation caused by the ELMs. The radiation bursts measured by the bolometer during the MHD-ELMs were poloidally asymmetric

in front of the LH launcher and exceeded a threshold value. This type of radiation was typically associated with electric arcs in the launcher. The protection system stopped the LH system.

There are several important practical questions, which require further attention. It is still not clear what mechanism triggers the release of an anomalously large number of neutral particles from the plasma-facing components. There is a clear sign of interaction of energetic electrons (E>2.2keV) with the first wall at the time of start of the MHD-ELM (Fig.13a). This interaction leads to a local increase in the soft X-ray emission and is accompanied by a long lasting temperature increase of the first wall material (Fig.16). This kind of interaction may cause a release of hydrogen and deuterium from the bulk volume of the first wall material. The role of the fast ions in the process is not clear. The scintillator probe detects enhanced losses of the energetic ions (250keV-3MeV) during MHD-ELMs. However, there is a time delay of the order of 100-200μs with respect to the D-alpha signal which makes fast ions an unlikely candidate for triggering the neutral gas release. There are no data on losses of the beam ions (E≤100keV).

The heat load on the outer target plate of the divertor is rather moderate during large MHD-ELMs as compared to the regular type-I ELMs (Fig.1,15, Table-1). The question remains as to what is the mechanism of the redistribution of the lost energy during this type of ELMs and how it could possibly be used?

There is a number of physical questions, which may shed a light on the mechanism of the formation of MHD-ELMs. It would be instructive, in particular, to investigate the role of high frequency modes (Fig.6a, 11a, 12)) present in the plasma prior to the ELM crash. The analysis of the non-thermal emission (Fig.11) should provide the information on the electron distribution function and possibly on the mechanism of energy and particle losses during an MHD-ELM.

To conclude we found that large ELMs triggered by MHD were observed in a considerable proportion of Advanced Scenario high β_N discharges. Specifically, large MHD-ELMs were found in low triangularity hybrid scenario and discharges with ITBs. They were not identified in the high triangularity hybrid scenario discharges. The impact of such ELMs on plasma performance and heating systems can be quite substantial. Large MHD-ELMs may deteriorate plasma confinement, cause intensive plasma wall interaction in the main chamber, cause influx of impurities and increase in Z_{eff} and in the edge plasma density as shown by the detailed analysis of the discharge discussed in this paper. The nature of the MHD excitation, which triggers large ELMs or disruptions in advanced scenario discharges has been discussed earlier [19]. It is connected to the safety factor, pressure profiles and fast particles population. One of the key questions is how to avoid the MHD leading to such large ELMs. One possible route is a development of the high triangularity hybrid scenario. Tailoring of the q-profile is another possibility. We believe that it is one of the most effective tools applicable to any type of advanced tokamak plasmas. A discussion of this problem, however, is outside of the scope of our investigation.

ACKNOWLEDGEMENTS

This work, part-funded by the European Communities under the contract of Association between EURATOM and CCFE, was carried out within the framework of the European Fusion Development Agreement. The views and opinions expressed herein do not necessarily reflect those of the European Commission. This work was also part-funded by the RCUK Energy Programme under grant EP/I501045.

REFERENCES

[1]. A. Loarte et al., Plasma Physics and Controlled Fusion **45** (2003) 1549.

[2]. A. Loarte, et al., Journal Nuclear Materials **962** (2003) 313.

[3]. E. Joffrin et al, High confinement hybrid scenario in JET and its significance for ITER, 23rd IAEA Fusion Energy Conference, 2010

[4]. J. Mailloux et al., Towards a Steady-State Scenario with ITER Dimensionless Parameters in JET, 23rd IAEA Fusion Energy Conference, 2010

[5]. V.V. Plyusnin et al., Enhancement of metal impurities release due to fast ions loss in JET. 11th IAEA Technical Meeting on Energetic Particles in Magnetic Confinement Systems, Kyiv, Ukraine, 2009

[6]. P. Mantica et al., Plasma Physics and Controlled Fusion **44** (2002) 2185

[7]. L. Barrera et al., Plasma Physics and Controlled Fusion **52** (2010) 085010

[8]. P. Buratti et al., Kink Instabilities in High-Beta JET Advanced Scenarios, 23rd IAEA Fusion Energy Conference

[9]. Cenacchi G. and Taroni A. 1988 JETTO: A free-boundary plasma transport code (basic version) *JET Report* JET-IR(88)03

[10]. J.Connor et al., Physics of Plasmas **5** (1998) 2687

[11]. Snyder P.B. *et al* 2005 Physics of Plasmas **12** 056115

[12]. K.K.Kirov et al., 2010 Nuclear Fusion **50** 075003

[13]. Darrow D.S. et al., Review of Scientific Instruments **75** (2004) 3566)

[14]. V.G.Kiptily et al., Nuclear Fusion **49** (2009) 065030

[15]. R.J. Goldston et al., Journal of Computational Physics **43** (1981) 61

[16]. T.Eich et al, Journal of Nuclear Material, accepted for publication (PSI-19)

[17]. W. Fundamenski et al., Effect of ion mass and charge on divertor heat load profiles on JET, 23rd IAEA Fusion Energy Conference.

[18]. V.G.Kiptily et al., Studies of MHD Effects on Fast Ions: towards Burning Plasma with ITER-like Wall on JET, 23rd IAEA Fusion Energy Conference

[19]. G.T.A.Huysmans et al., Nuclear Fusion **39** (1999) 1489

Time (s)	W_{dia} (MJ)	ΔW_{dia} (MJ)	E_{rad} (MJ)	E_{drad} (MJ)	E_{t5} (kJ) $\Delta t = 1.5ms$	max (T_{out}) (deg)
5.107	6.8	0.25	0.14	0.1	60kJ	1910
5.201	6.8	0.80	0.44	0.32	73kJ	1850

Table I : Comparison of various energy losses during a regular Type I ELM and a large MHD-ELM. Diamagnetic energy before ELM- W_{dia} and its variation during ELM- ΔW_{dia}, total- E_{rad} and energy radiated in the divertor E_{drad} during 5ms from the start of ELM, E_{t5}-energy dissipated on the outer target plate of the divertor (tile 5), T_{max}-maximum surface temperature of the outer target plate of the divertor.

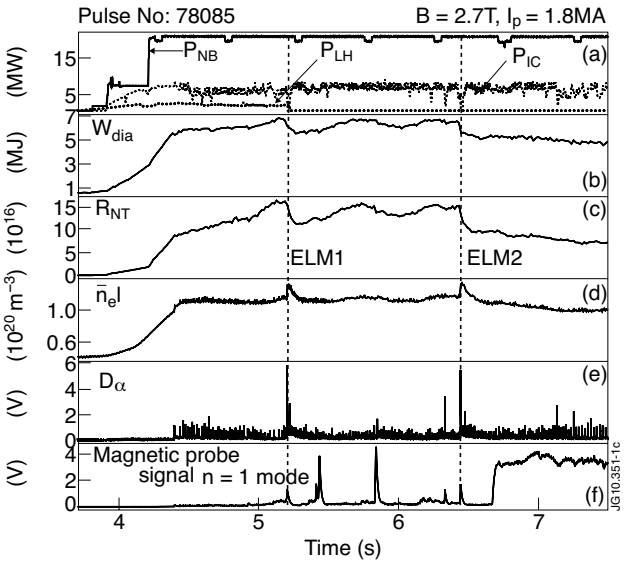

Figure 1: Evolution of the main plasma parameters. a) neutral beam power-PNB, ICRH power-PIC, LH power-PLH b) diamagnetic energy Wdia c) neutron yield-RNT d) integrated density along the central vertical line of sight e) D-alpha signal f) magnetic probe signal for n=1 mode. Large MHD-ELMs are marked as ELM1 and ELM2. Pulse No: 78085, magnetic field B = 2.7T and plasma current I_p = 1.8MA.

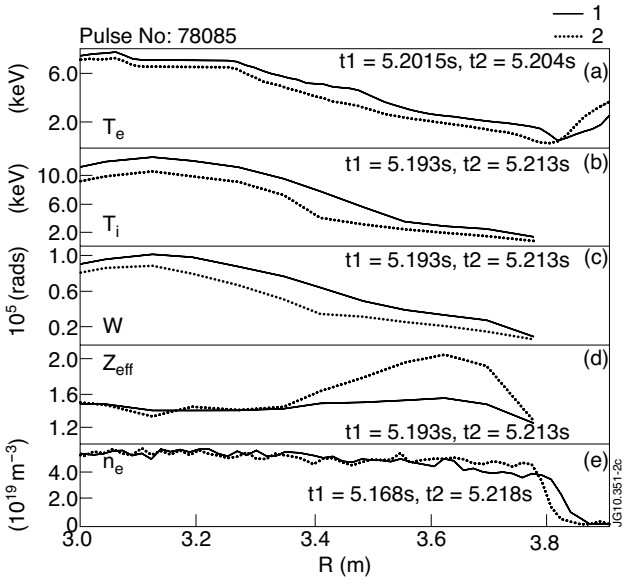

Figure 2: Profiles of electron, ion temperatures, toroidal rotation frequency, effective plasma charge and electron density before and after ELM1 triggered by MHD. Pulse No: 78085.

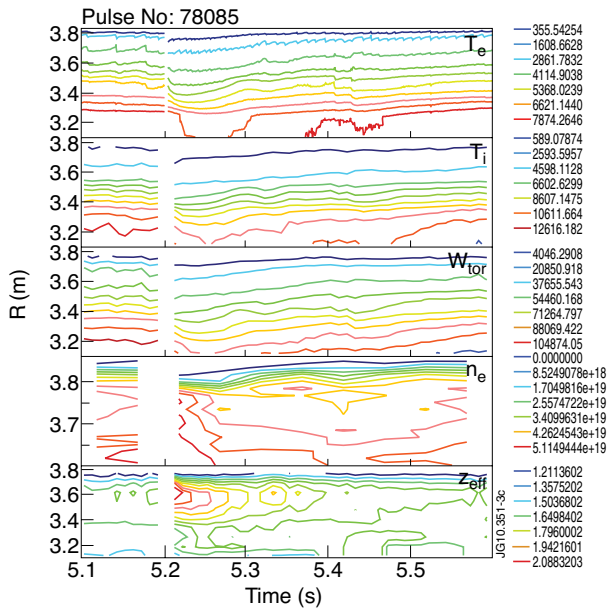

Figure 3: Contour plot of electron and ion temperatures, toroidal rotation frequency, electron density and effective plasma charge. The gap corresponds to the time interval around MHD-ELM, when the data are not available. Sharp variation during the ELM and variation on a diffusive time after the ELM are clearly seen. Pulse No: 78085.

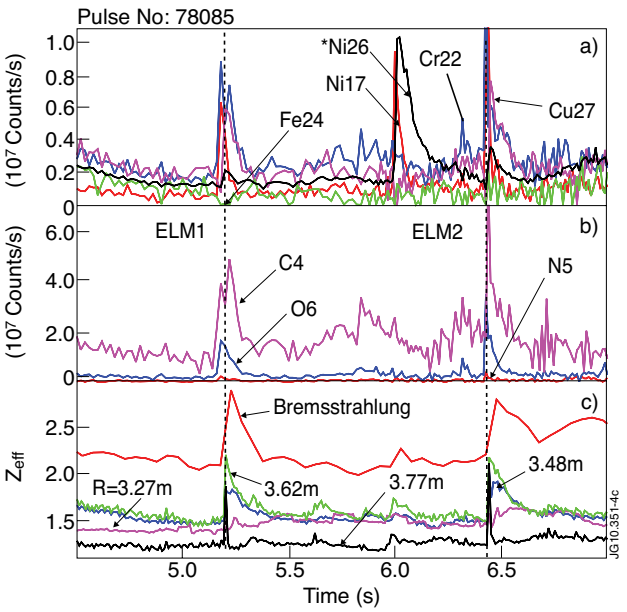

Figure 4: a) Intensity of the emission of the a) heavy and b) light impurity lines and c) Z_{eff} variation. Z_{eff} at different radii was measured by CX diagnostic, which reflects a contribution of C does not take into account heavy impurities. Pulse No: 78085.

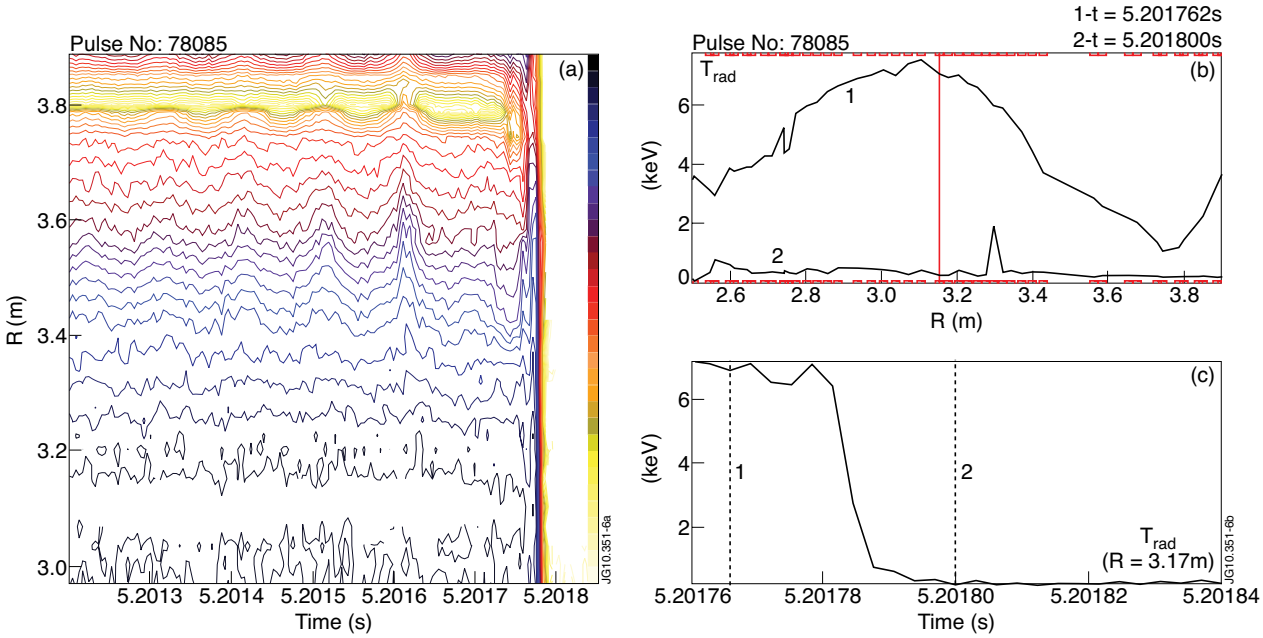

Figure 5: a) Contour plot of the radiation temperature Trad measured by Heterodyne Radiometer at the second harmonic of the X-mode. Contour label is in keV. Trad perturbation becomes larger after t=5.2016s and they destroy the separatrix with a subsequent collapse of the T_{rad}. b) Trad before the ELM1 crash and 20μs after the crash. c) Time variation of Trad at a fixed R=3.15m. Pulse No: 78085.

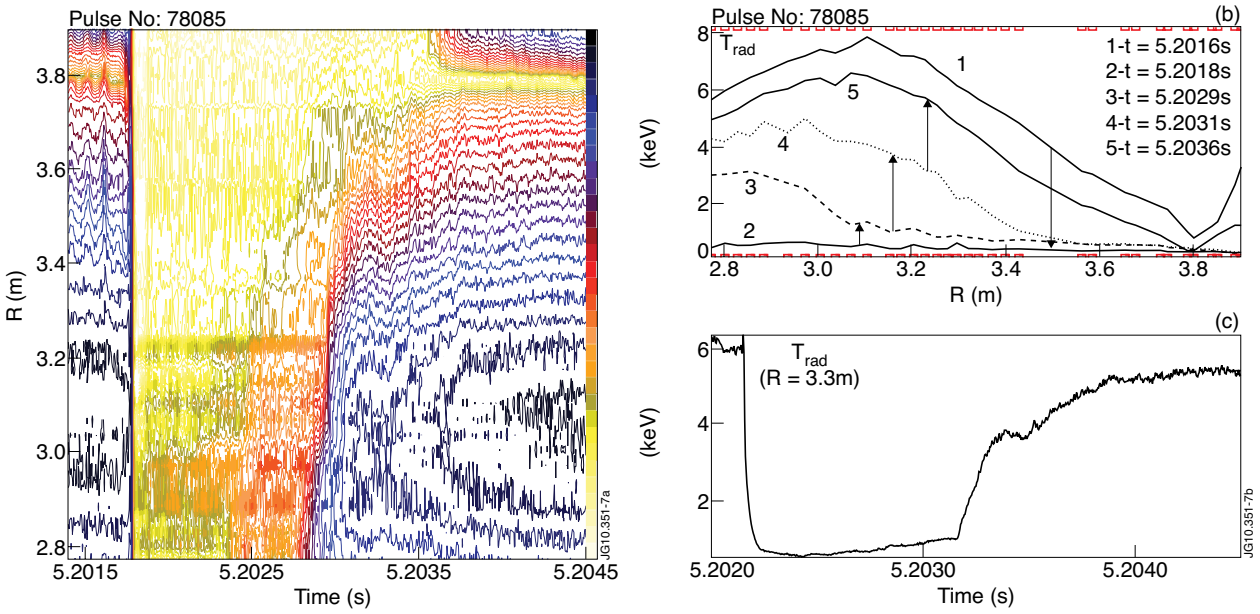

Figure 6: a) Contour plot of the radiation temperature Trad measured by Heterodyne Radiometer at the second harmonic of the X-mode. Contour label is in keV. b) Trad before the ELM1 crash, during the black out and recovery of the ECE emission. C) Time variation of Trad at a fixed R=3.3m. Pulse No: 78085.

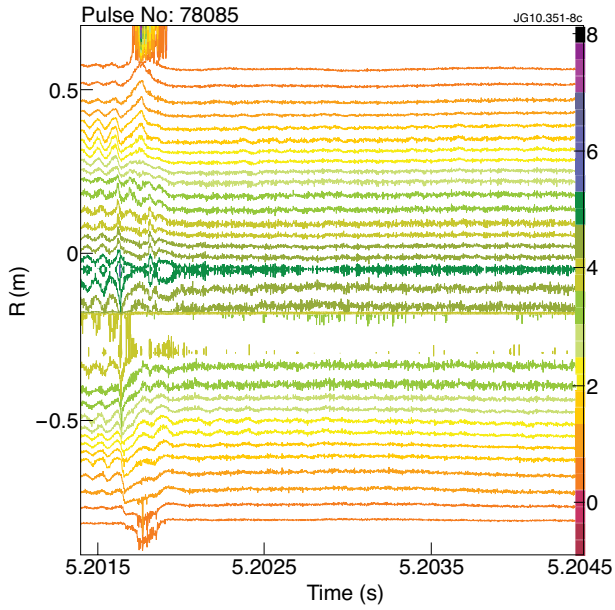

Figure 7. Contour plot of soft X-ray emission during ELM1 triggered by MHD. Horizontal camera. Contour labels-kW/m^2. The amplitude of the radiation is reduced in 200-300ms after t = 5.2017s and radiation profile shrinks. There is no visible change in the radiation after t = 5.202s, which testifies that Te does not change significantly. Pulse No: 78085.

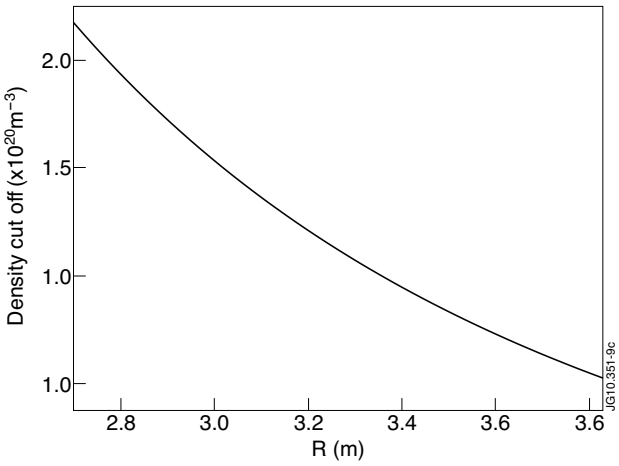

Figure 8: The cut-off electron density at the separatrix location R = 3.8m for the second harmonic of the X-mode of ECE emission frequency. The cut-off density is a function of the emission frequency $\omega = 2\omega_{ce}(r) = 2eB(r)/mc$. The radiation is assumed to be propagating perpendicular to the magnetic field in the equatorial plane. Pulse No: 78085, t = 5.201s.

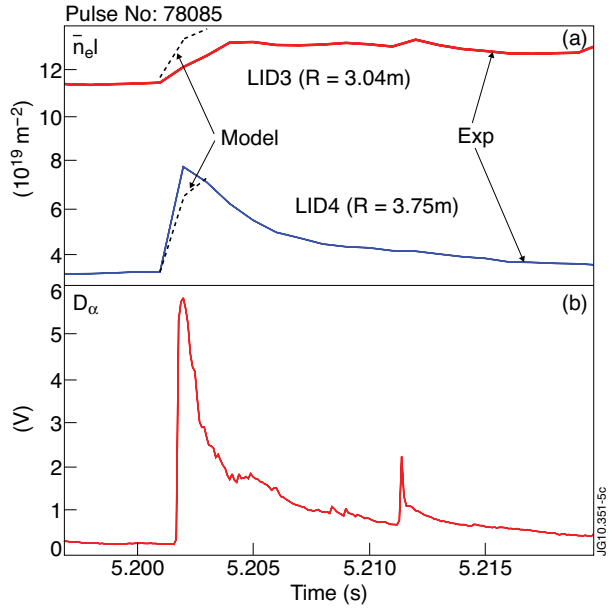

Figure 9: a) Variation of the line integrated density measured by interferometer during ELM1 triggered by MHD. b) Dα signal measured along the vertical line of sight. Pulse No: 78085.

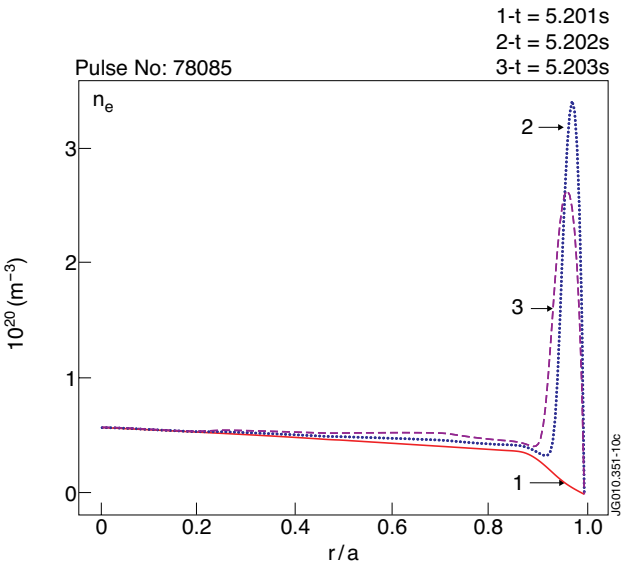

Figure 10: Results of JETTO modelling for electron density variation during ELM triggered by MHD. The neutral gas flux was assumed to be increasing from 3×10^{22}el/s to 5×10^{24}el/s during time interval t= 5.2015s-5.202s and then decreasing to the initial level. Small particle diffusion coefficient D=1m^2/s was used to estimate the minimum amount of neutral gas required to increase the peripheral density in a short period of time above the cut-off level. Pulse No: 78085

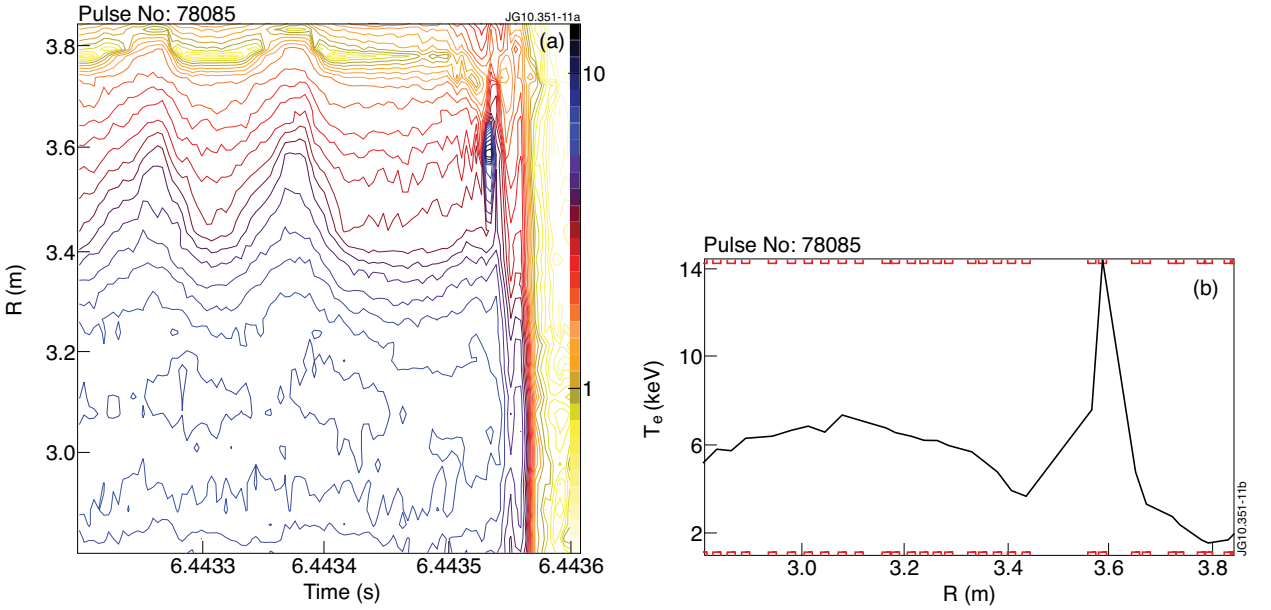

Figure 11: a) Contour plot of the radiation temperature Trad measured by Heterodyne Radiometer at the second harmonic of the X-mode. Contour label is in keV. A formation of high frequency perturbations after t = 6.4434s can be seen in the region R = 3.5–3.6m. These perturbations propagate towards the separatrix and destroy it. b) Trad before the ELM1 crash. A burst of non-thermal emission occurs around R = 3.6m. Pulse No: 78085.

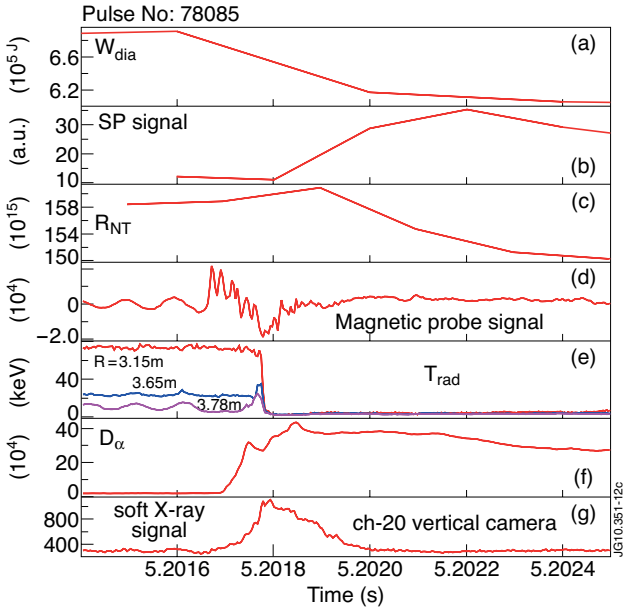

Figure 12: A variation of the diamagnetic energy, fast ion losses, neutron yield, magnetic probe signal, Trad at different radii, D-alpha and soft X-ray emission signal during ELM1. The D-alpha signal increases at the time of the fragmentation of the original global kink-mode ($t < 5.2016$s) into high frequency mode on the magnetic probe signal ($t > 5.2016$s). The electron density at the edge, probably, starts to rise simultaneously with D-alpha signal and it reaches the cut-off density (see Fig.9) at the time, when Trad drops to a low level below 1keV. The fast ion losses increase measured by SP, surprisingly, delayed with respect to MHD signal. It reaches a maximum value at the time when MHD activity is reduced to the noise level. Crosses in (a),(b) and (c) indicate experimental points. The time resolution of other signals is of the order of 10μs and not shown in the graph. Pulse No: 78085.

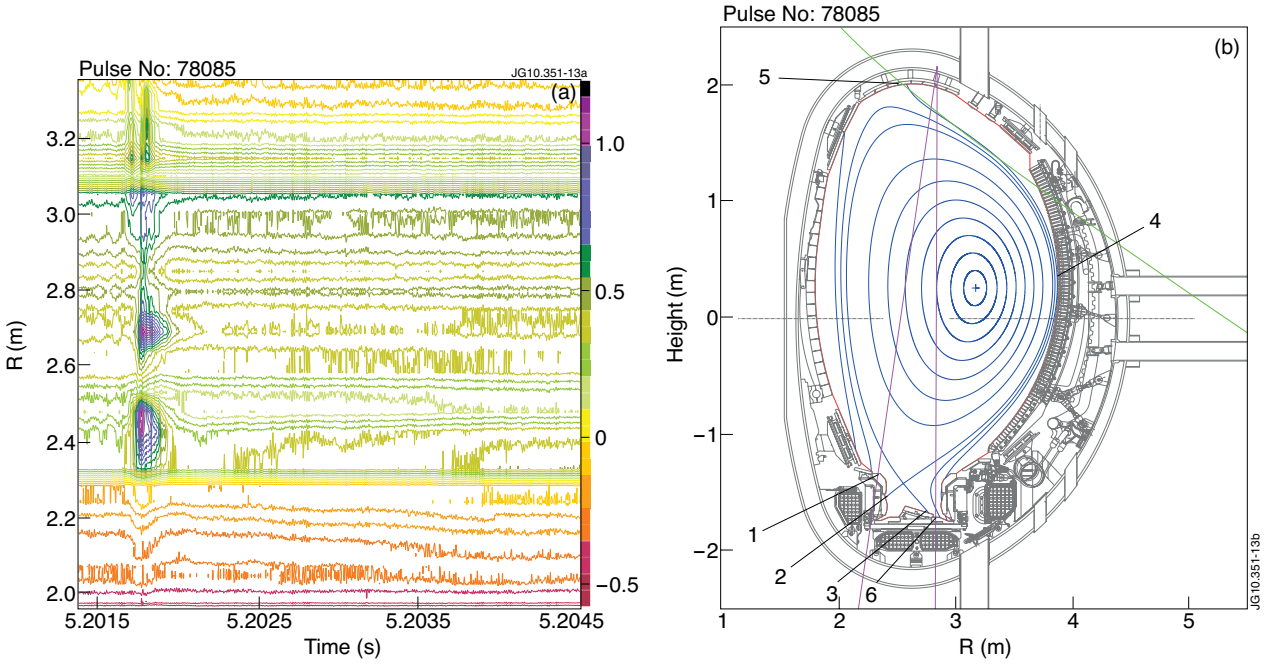

Figure 13. a) A contour plot of the soft X-ray emission measured by vertical camera during ELM1. Colour label is kW/m2. b) The tokamak cross-section. Bright spots occur at the start of the ELM1 on the emission contour plot (a) at $t \approx 5.2017$s and $R \approx 2.45$m and 2.7m. These bright spots are detected by the camera along two vertical lines of sight shown in (b). These lines cross the plasma facing components at points 1 above the diverter and point 6 on the divertor outer target plate. Similar bright spot is registered the horizontal camera at $R \approx 0.65$-0.7m as can be seen in Fig.8. Corresponding line of sight crosses the main chamber wall at point 5 as shown in (b). Pulse No: 78085.

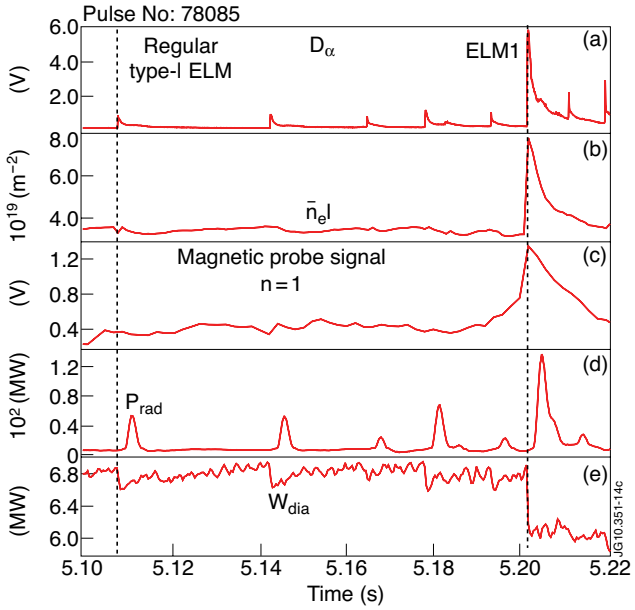

Figure 14: Comparison of regular type-I ELMs with the ELM triggered by MHD. Frequency filter introduces artificial time delay of the order of 2ms in the bolometer signal P_{rad}. Pulse No: 78085.

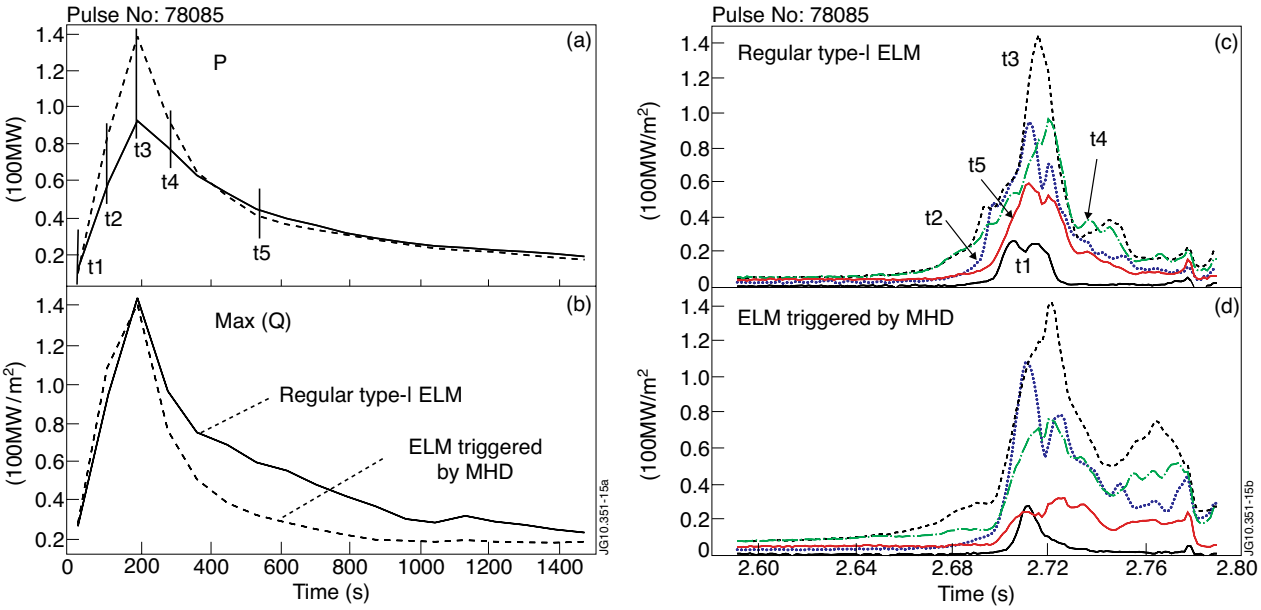

Figure 15: Comparison of regular type-I ELM and ELM triggered by MHD (ELM1). a) Total heat flux on the divertor outer target plate, b) maximum of the heat flux on the outer target plate, c,d) radial profiles of the heat flux on the outer target plate for different time slices. The time slices are indicated in a. Note, the heat flux integrated over 1.5ms is 20% bigger, but the maximum flux is smaller on average for ELM1 than for regular type-I ELM, respectively. Pulse No: 78085.

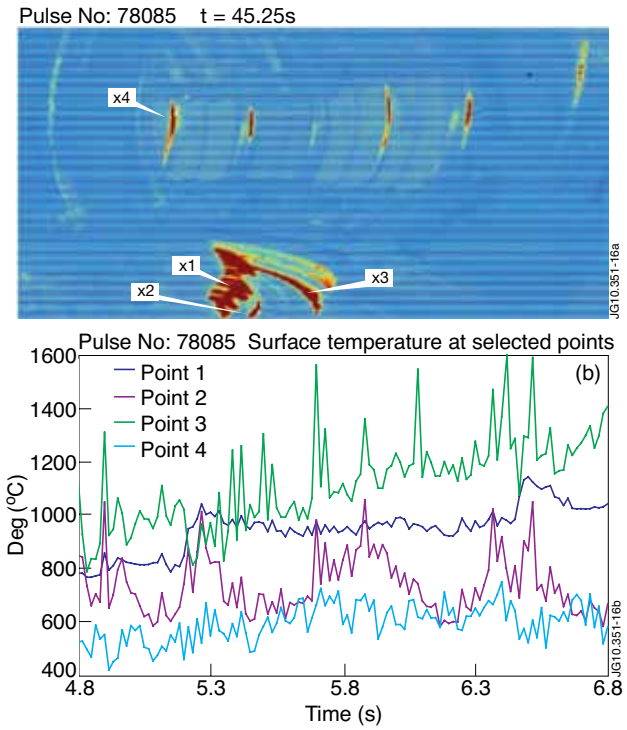

Figure 16: a) Infra-red camera view, b) surface temperature at four points marked in a. Figure 13b shows the points location in the tokamak cross-section. Note, that temperature experience considerable jumps at the location 1 (above the divertor) and 2 (inner striking point) after the ELM1 and ELM2. The temperature remains elevated for about 1s at the point 1 and decreases faster at point 2. Temperatures at the point 3 (outer striking) and 4 (ICRH antenna septum) are not affected significantly by ELM1 or ELM2. Pulse No: 78085.

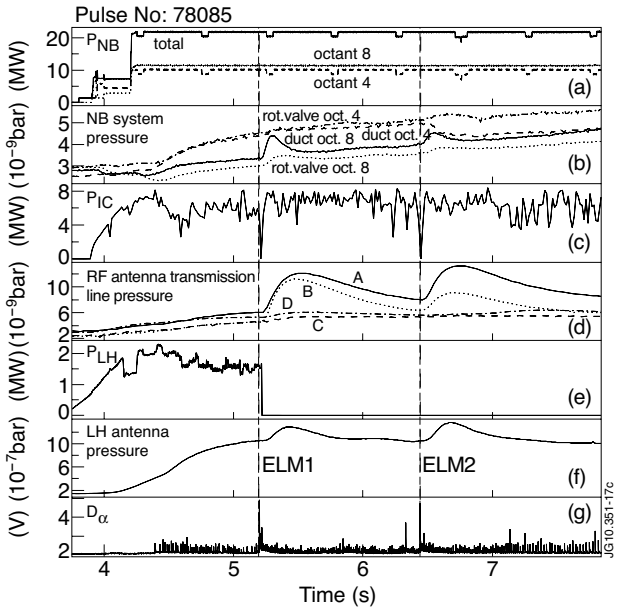

Figure 17: a) NB power total in different octants, b) neutral gas pressure in the ducts and rotary valves of the NB system, c) ICRH power, d) pressure inside the ICRH transmission line system for different antennae (A,B,C,D), e) LH power, f) pressure inside the LH antenna, g) D-alpha signal. ELMs triggered by MHD are marked by vertical dashed lines. Both ELM1 and ELM 2 trip IC and LH power. The neutral gas pressure rises considerably after both ELMs. The real increase is significantly larger than the signal from the pressure monitor due to its integration properties. The pressure increases only in the duct and rotary valve of octant 8 indicating the toroidal asymmetry in the pressure inside the vacuum vessel. Similar asymmetry is observed in the pressure inside the ICRH transmission lines. Pulse No: 78085.

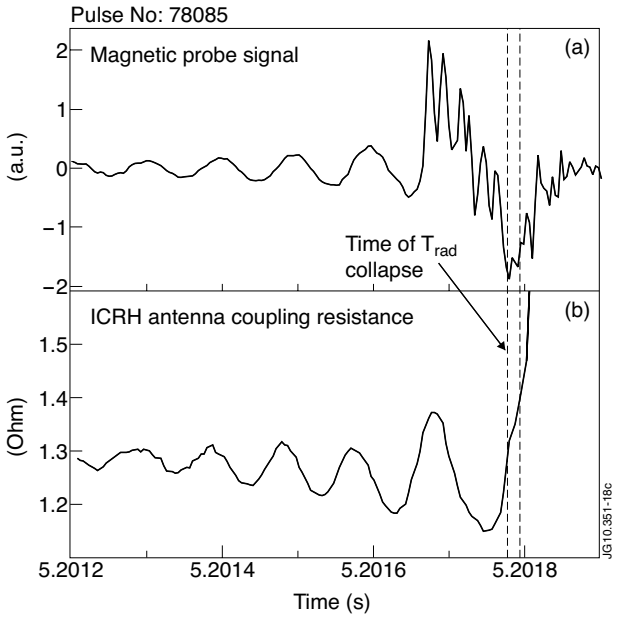

Figure 18: a) Magnetic probe signal and b) ICRH antenna coupling resistance during large MHD-ELM (ELM1). Pulse No: 78085.

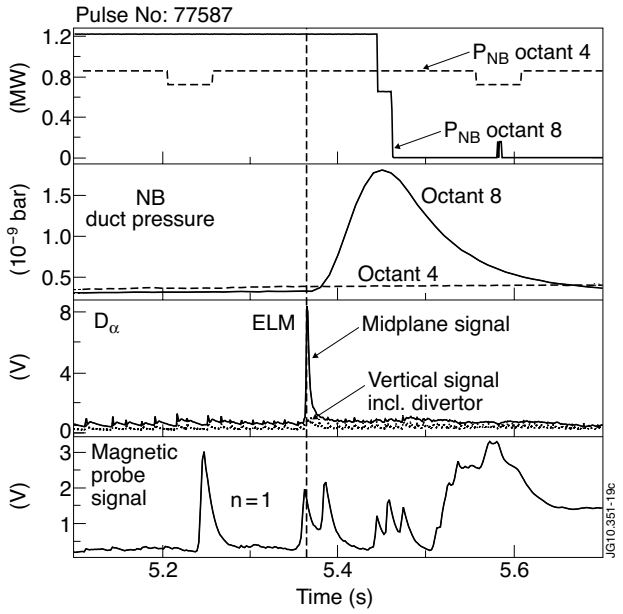

Figure 19: a) NB power in octants 4 and 8, b) NB duct pressure, c) D-alpha signal, d) magnetic probe signal for n=1 mode. Pulse No: 77587